



Alexandria University  
**Alexandria Engineering Journal**

[www.elsevier.com/locate/aej](http://www.elsevier.com/locate/aej)  
[www.sciencedirect.com](http://www.sciencedirect.com)



# Fluid-structure interaction model of blood flow in abdominal aortic aneurysms with thermic treatment

Ammar I. Alsabery<sup>a</sup>, Muneer A. Ismael<sup>b</sup>, Saleem K. Al-Hadraawy<sup>c</sup>,  
 Mohammad Ghalambaz<sup>d</sup>, Ishak Hashim<sup>e,\*</sup>, Ali J. Chamkha<sup>f</sup>

<sup>a</sup> Refrigeration & Air-conditioning Technical Engineering Department, College of Technical Engineering, The Islamic University, Najaf, Iraq

<sup>b</sup> Mechanical Engineering Department, Engineering College, University of Basrah, Basrah, Iraq

<sup>c</sup> Department of Biology, College of Sciences, University of Kufa, Najaf, Iraq

<sup>d</sup> Laboratory on Convective Heat and Mass Transfer, Tomsk State University, 634045 Tomsk, Russia

<sup>e</sup> Department of Mathematical Sciences, Faculty of Science & Technology, Universiti Kebangsaan Malaysia, 43600 UKM Bangi, Selangor, Malaysia

<sup>f</sup> Faculty of Engineering, Kuwait College of Science and Technology, Doha District 35004, Kuwait

Received 18 March 2022; revised 6 July 2022; accepted 22 August 2022

## KEYWORDS

Forced convection;  
 Heat transfer;  
 Carreau non-Newtonian model;  
 Blood flow;  
 Fluid–structure interaction;  
 Abdominal aortic aneurysms

**Abstract** Hyperthermia is one of the non-invasive therapy of an Abdominal Aortic Aneurysm (AAA), which is achieved by applying a heat source upon the AAA without surgical operation. This research paper considers laminar flow and heat transfer in a heated abdominal aortic aneurysm using an isothermal boundary condition. Heat is added to explicate the thermal treatment of a diseased artery. The blood is assumed as a non-Newtonian fluid based on the shear-thinning Carreau model. Two unequal aneurysms are assumed in the lower wall to simulate bulges or a disordered artery. Flexible wall segments are assumed in the upper wall and opposing to each aneurysm. The transient momentum and energy equations are solved based on the fluid–structure interaction (FSI) using the Arbitrary-Lagrangian–Eulerian (ALE) method. It is found that the shear stress is much higher for a higher index of the power-law fluid governing the blood viscosity and hence, it is strictly recommended to reduce the viscous nature of the blood in diseased vessels. It is found also that the thermal energy can be greatly transported across the blood at a higher Reynolds number, this means that the hyperthermia therapy becomes effective when blood flows violently through the aortic.

© 2022 THE AUTHORS. Published by Elsevier BV on behalf of Faculty of Engineering, Alexandria University. This is an open access article under the CC BY-NC-ND license (<http://creativecommons.org/licenses/by-nc-nd/4.0/>).

\* Corresponding author.

E-mail addresses: [m.ghalambaz@gmail.com](mailto:m.ghalambaz@gmail.com) (M. Ghalambaz), [ishak\\_h@ukm.edu.my](mailto:ishak_h@ukm.edu.my) (I. Hashim).

Peer review under responsibility of Faculty of Engineering, Alexandria University.

<https://doi.org/10.1016/j.aej.2022.08.032>

1110-0168 © 2022 THE AUTHORS. Published by Elsevier BV on behalf of Faculty of Engineering, Alexandria University. This is an open access article under the CC BY-NC-ND license (<http://creativecommons.org/licenses/by-nc-nd/4.0/>).

## 1. Introduction

One of the important topics that has received a great attention in the past decades is the heat exchange between man and his

**Nomenclature**

$d$	dimensional length of the heater (m)
$d_s^*$	displacement vector (m)
$D_{ij}$	components of the rate of the deformation tensor
$E$	dimensionless Young's modulus
$F_v$	dimensionless body force vector
$g$	gravitational acceleration
$h$	height of the channel
$k$	thermal conductivity
$K_r$	thermal conductivity ratio of the solid to the fluid
$L$	length of the channel
$n$	power law index
$\mathbf{n}, \mathbf{n}$	unit vector (m)
$\overline{Nu}$	average Nusselt number
$p$	pressure (N m <sup>-2</sup> )
$Pr$	Prandtl number
$Re$	Reynolds number
$S$	stress tensor
$t$	dimensionless time
$T$	temperature
$u^*, w^*$	fluid velocity vector and moving coordinate velocity (m s <sup>-1</sup> )
$x, y$	space coordinates (m)

*Greek symbols*

$\alpha$	thermal diffusivity
$\beta$	thermal expansion coefficient
$\dot{\gamma}$	tensor of strain rate
$\lambda$	time constant
$\varepsilon$	strain
$\theta$	dimensionless temperature
$\mu$	dynamic viscosity
$\mu_0^*$	asymptotic viscosity at zero shear rate
$\mu_\infty^*$	asymptotic viscosity at infinite shear rate
$\nu$	kinematic viscosity
$\rho$	density
$\sigma$	dimensionless stress tensor
$\tau$	dimensionless period of oscillation

*subscript*

$c$	cold
$f$	fluid
$h$	hot
$in$	inlet
$r$	the property ratio of the solid to the fluid
$s$	solid
$out$	outlet

environment. There are environments with few extremes, but they pose a major threat to human health [1]. Aorta is a major vessel of transporting blood between the main parts of human body. When the walls of the aorta get weak, abdominal aortic aneurysm (AAA) phenomenon may occur, where the walls swell like balloon [2]. An alternative way to treat AAA is by applying a heat source upon the location of the aorta defect, which is known as a non-invasive local hyperthermia [3]. On the other hand, in order to collect the data necessary for the actual thermal behavior and simulate response of men and women, physiological studies must be carried out during a human exposure to harsh environmental conditions [4,5], as these studies are used to create important and basic databases in theories of heat regulation, a variety of models that mimic thermal behavior have been developed. The pattern and components of blood flow depend mainly on the relationship between the flow conditions and the characteristics of the blood, which may lead to blockages and rupture of blood vessels. This explains the role of the behavior of the blood vessel walls and their movement in narrowing and blocked of vessels [4]. Saleem et al. [6] considered the peristaltic flow in an irregular wavy channel to simulate different actions of in human body such as the conveyance of the urine from the kidney to the bladder and transformation of food bolus through the esophagus and many other actions. They considered the flow is due to the pressure gradient and the slip is partially occurred. The outcomes were that the pressure gradient increases with the waviness of the channel wall, but the slip parameter is vice versa. They showed also that the flow velocity is boosted by a bit increase in the wave number while it is declined by a rise in the slip parameter.

It is an important natural phenomenon practiced by researchers in recent years theoretically and experimentally which has great benefits in industrial applications and is one of the visual phenomena that have been used in the field of biomedicine and medical, mechanical and chemical applications. Most of the investigations and clinical applications carried out by the researchers showed the effects of heat on the rate of fluid absorption [7] as a result of the formation of an alternating magnetic field for all samples that contain magnetic particles, and this depends on the rate of heat heating [8] where some scientists have studied the physical properties of solid samples to reach Effects of heat heating on magnetic fluids. Wakif [9] performed novel mathematical computations to analyze the MHD radiative convective flow Casson fluids moving over a nonlinearly elongating elastic sheet with a non-uniform thickness. His main finding is that the fluid motion can be strengthened slightly near the stretching sheet either by decreasing the Prandtl number or by escalating the values of radiation, wall thickness and thermal conductivity parameters. While away from the stretching sheet, these parameters act in opposite dynamical features. Ashraf et al. [10] conducted a numerical investigation of a wavy channel of solid walls to represent a vessel of blood flow under the assumption of Casson fluid. They incorporated platelet-shaped magnetite nanoparticles of Fe<sub>3</sub>O<sub>4</sub> to undergo the applied magnetic field. They reported that the heat transfer rate enhances by increasing the volume fraction of the magnetite nanoparticles, while the skin-friction coefficient and Nusselt number increase by enhancing the strength of the magnetic field.

Some researchers have attempted to study the relationship between cancer and the distribution of temperature in the

affected tissue by studying the relationship between the concentration of nanoparticles on the distribution of temperatures in the affected tissue [11] as well as the effects of magnetic field strength and nanoparticle sizes on the distribution of temperatures within a living tissue [12]. Some scientists have examined the study of the effect of some physical properties on the microscopic structures of tissues such as the effect of heating and concentration of magnetic particles and its effect on the alternating magnetic field of these particles [13,14]. Many researchers have studied in the field of application of magnetic dynamics the relationship of blood flow to the magnetic field. Saranya and Al-Mdallal [15] inspected the comparison between heat transfer Casson fluid and MHD flow. The Casson flow was used to account for non-Newtonian base fluid with three types of ferroparticles. The flow of the non-Newtonian ferrofluids and the applied magnetic field are both perpendicular and over an unsteady contracting cylinder. They found that the aligned angle parameter and magnetic parameter increase the rate of heat transfer while the unsteadiness parameter exhibit opposite action. Midya et al. [16] concluded that the magnetic field of blood in the expansion area. Also, others concluded that the intensity of the magnetic field in the contraction area increases the area of contraction and reduces blood flow in the contraction zone [17]. It was also noted that magnetic fields contribute to raising temperatures that are effective in treating wounds much shorter than in the absence of the magnetic field [18]. Chinyoka and Makinde [19] studied the axial pressure gradient under the influence of the magnetic field and the thermal radiation affecting the speed.

Although all previous studies considered blood to be a liquid subject to Newton's law, in reality it is a fluid called plasma in which a number of cells swim such as red blood cells, white blood cells, and platelets in which blood is a non-Newtonian viscous fluid, flexible with a variable flow [20]. However, some researchers considered the blood as a Newtonian fluid such as [21] the pulsating blood flow in the ventral aortic part commensurate with the expansion of the blood vessels, while some studies have proven under constant flow conditions that there are numerical simulations of blood flow in the ventral aortic part [22,23]. Wakif et al. [24] implemented efficient numerical techniques to study the boundary layer flows driven by the stretching motion of flat surfaces. They applied rigorous physical theories and assumptions to explore the main consequences arising from the convective motion of micropolar nanofluid medium including 60% of ethylene glycol, 40% of pure water, and a certain volume fraction of alumina nanoparticles. They deduced the improvement of the temperature of the micropolar nanofluidic medium with an enrichment in the rate of wall heat transfer when with the loading of nanoparticles.

The aorta is the human body's major blood vessel that passes blood from the heart to lower body parts through the abdomen. The local enlargement of this vessel in the abdominal area could lead to an abdominal aneurysm. When an aneurysm occurs, the vessel wall weakens, and due to the widening (dilation) of the artery, a vessel rupture could happen. The literature review shows that 5% to 10% of men aged between 65 and 79 have an abdominal aorta aneurysm [25]. The aneurysms of this vessel do not show much of symptoms, but its rupture could be lethal. When the rupture occurs, the mortality rate could be as high as 80% [26,27]. Abdominal aor-

tic aneurysms are responsible for the deaths of 13% of men aged 65–85 years in developed countries [28]. Thus, elective surgery repair will be required to prevent death due to rupture. In some cases of growing aneurysms, monitoring of patient conditions for emergency surgery is required [25]. The aneurysms can be repaired by an open surgery and an endovascular surgery [29]. In an endovascular surgery, a surgeon performs tiny cuts and places long-thin tubes, catheters, to repair the vessel. The literature review shows that the endovascular approach could lead to a better outcome in the short term compared to an open surgery. However, it could lead to long-term complications partially due to endograft ruptures in terms of death in the long-term. Thus, modeling and simulation of aneurysm vessels is an important task which adds knowledge to the physical interaction of blood and an aneurysm vessel. The simulations could also use as an opportunity to better decide about an elective surgery repair and the surgery method.

The vessel is an elastic medium which could be deformed due to interaction with the blood flow. The deformation of the vessel will change the shape of the vessel, and thus, there is a two-way coupling between the blood flow and the deformation of the vessel. The Fluid-Structure Interaction (FSI) approach is a technique that utilizes the moving mesh method to track the deformation of a structure due to its interaction with a flow. Using FSI, the two-way coupling between the flow field and the structure is possible. The heat transfer between the blood flow and the abdominal section is another physical phenomenon that takes place when the body is subject to rapid temperature changes. Recently, the FSI approach has been successfully applied in some of the industrial flow and heat transfer applications, such as chambers with flexible walls [30,31], and enclosures with flexible membranes. Kumawat et al. [23] presented a numerical study of analyzing the entropy generation of MHD blood flow through a permeable curved artery with constriction. They considered the effect of heat and chemical reaction. The flow of blood was taken as two-phases; core and plasma region. Their results suggested that the risk of atherosclerosis formation rises due to the permeability and curvature of the arterial wall, whereas the heat source on the blood flow lower this risk.

The aim of the present study is to simulate the hyperthermia therapy of AAA by making a CFD analysis of non-Newtonian blood flow and heat transfer in an a flexible elastic channel with using the FSI approach. The aim is to answer the following fundamental questions: what is the impact of blood flow rate (Reynolds number) on the aneurysm growth in the channel? How could the non-Newtonian power-law fluid index impact the aneurysm growth and the flow behavior? What is the relation between the non-Newtonian power-law index of blood flow and the induced stress on the aneurysm channel walls?.

## 2. Mathematical Formulation

The considered problem is two local enlargements of aorta (two aneurysms) with their sizes changing with time and according to the strength of the blood flow. To simplify the computations by a 2D geometry, the two aneurysms are assumed azimuthally symmetric and the lower parts are permanently swollen, while the upper swell according to the blood

flow. The hyperthermia therapy is simulated by heating the lower walls by a high temperature  $T_h$ . The problem is solved transiently. Due to the forced blood flow, the problem is classified as a forced convection flow and heat transfer. The channel height is  $h$  and its length is  $L$  (see Fig. 1). Two flexible surfaces are embedded into the top surface of the channel over a length of  $0.4L$  and  $0.6L$ . These segments are considered very thin with a thickness of  $0.012h$  and an elasticity modulus,  $E^*$ . The fluid is considered as a non-Newtonian blood and the flow is incompressible. By neglecting the buoyancy force within the channel, all physical properties of the fluid and the flexible wall are assumed unchanged. The dimensional unsteady governing equations of the laminar fluid in vector form in the Arbitrary Lagrangian–Eulerian procedure (ALE) are written as [20,31]:

$$\nabla \cdot u^* = 0, \quad (1)$$

$$\frac{\partial u^*}{\partial t^*} + (u^* - w^*) \cdot \nabla u = -\frac{1}{\rho_f} \nabla p + \frac{1}{\rho_f} \nabla \bar{\tau}, \quad (2)$$

$$\frac{\partial T}{\partial t^*} + (u^* - w^*) \cdot \nabla T = \alpha_f \nabla^2 T, \quad (3)$$

where  $u^*$  is the fluid velocity vector,  $w^*$  is the moving coordinate velocity,  $\rho_f$  the fluid density and  $T$  is temperature. Considering generalized incompressible non-Newtonian fluids, the dimensionless stress tensor is [32]:

$$\tau = \tau_{ij} = 2\mu^*(\dot{\gamma})D_{ij}, \quad (4)$$

where  $\mu^*(\dot{\gamma})$  is the generalised non-Newtonian viscosity,  $\dot{\gamma}$  is the rate-of-strain tensor (with magnitude  $\dot{\gamma} = (2D_{ij}D_{ji})^{1/2}$ ) and  $D_{ij} = 0.5(u_{ij}^* + u_{ji}^*)$ . In the Carreau model [32],

$$\mu^* = \mu_\infty^* + (\mu_0^* - \mu_\infty^*) \left[ 1 + (\lambda^* \dot{\gamma})^2 \right]^{\frac{(n-1)}{2}}. \quad (5)$$

Here  $\mu_0^*$ ,  $\mu_\infty^*$ ,  $\lambda^*$  and  $n$  are, respectively, the zero-shear-rate viscosity, infinite-shear-rate viscosity, time constant and power-law index. The relationship between the stress tensor and deformation tensor of Carreau fluid flow in the high shear rate region is nonlinear [33]. Setting  $n = 1$  and  $\mu_0^* = \mu_\infty^*$  recovers the Newtonian fluid case. Since the value of  $\mu_\infty^*$  is about  $10^3 - 10^4$  times smaller than  $\mu_0$ , we fix  $\mu_\infty/\mu_0 = 0.001$ .

Also, the dimensional unsteady governing equations concerning the flexible portion are arranged within a vector pattern as follows [31]:

$$\rho_s \frac{d^2 d_s^*}{dt^{*2}} - \nabla \sigma^* = F_v^*, \quad (6)$$

$$\frac{\partial T}{\partial t^*} = \alpha_s \nabla^2 T, \quad (7)$$

where  $\rho_s$ ,  $\sigma^*$ ,  $d_s^*$ ,  $F_v^*$  and  $\alpha_s$  are the solid density, stress tensor, solid displacement vector, applied body force and the thermal diffusivity of solid respectively. Considering the wall as linearly elastic, the stress tensor is

$$\sigma = J^{-1} F S F^T, \quad F = (1 + \nabla^*), \quad J = \det(F). \quad (8)$$

The second Piola–Kirchhoff stress tensor  $S = C : (\varepsilon)$  where  $\varepsilon = \frac{(\nabla d_s^* + \nabla d_s^{*T} + \nabla d_s^{*T} \cdot \nabla d_s^*)}{2}$  and  $C = C(E^*, v)$ . On the flexible surfaces we have the following conditions

$$\frac{\partial d_s^*}{\partial t^*} = u^*, \quad \sigma^* \cdot n = -p + \mu^* \nabla u^*, \quad k_f \frac{\partial T}{\partial n} = k_s \frac{\partial T}{\partial n}. \quad (9)$$

Using the following dimensionless variables

$$(X, Y) = \frac{x, y}{L}, \quad (D, H) = \frac{(d, h)}{L}, \quad (u, v) = \frac{(u^*, v^*)}{u_{in}}, \quad w = \frac{w^* L}{\alpha_f}, \quad (10)$$

$$\theta = \frac{T - T_c}{T_h - T_c}, \quad d_s = \frac{d_s^*}{L}, \quad \sigma = \frac{\sigma^*}{E^*}, \quad t = \frac{t^* \alpha_f}{L^2}, \quad \tau = \frac{\bar{\tau}}{\rho_f \mu_{in}^2}, \quad P = \frac{p}{\rho_f \mu_{in}^2},$$

gives

$$\nabla \cdot u = 0, \quad (11)$$

$$\frac{\partial u}{\partial t} + (u - w) \cdot \nabla u = -\nabla P + \frac{\mu_a}{Re} \nabla^2 u + \frac{2D_{ij}}{Re} \nabla \mu_a, \quad (12)$$

$$\frac{\partial \theta}{\partial t} + (u - w) \cdot \nabla \theta = \frac{1}{Re \cdot Pr} \nabla^2 \theta, \quad (13)$$

$$\frac{1}{\rho_r} \frac{d^2 d_s}{dt^2} - E \cdot \nabla \sigma = E \cdot F_v, \quad (14)$$

$$\frac{\partial \theta}{\partial t} = \alpha_r \cdot \nabla^2 \theta, \quad (15)$$

where  $\mu_a = \mu^* \dot{\gamma}$  is the apparent viscosity,  $Re = \frac{\rho_f u_{in} L}{\mu^*}$  is Reynolds number,  $Pr = \frac{\mu^*}{\rho_f \alpha_f}$  is the Prandtl number,  $E = \frac{E^* L^2}{\rho_f \alpha_f^2}$  is the flexibility parameter, and  $\rho_r = \frac{\rho_f}{\rho_s}$ ,  $\alpha_r = \frac{\alpha_f}{\alpha_s}$  are the density ratio and the thermal diffusivity ratio, respectively.

Initially, the cavity connected to the hot surface and the cold inlet velocity which are respectively at uniform temperatures of  $T_h$  and  $T_c$ , and the fluid is quiescent (i.e.  $u^* = 0$ ). The dimensionless boundary conditions of Eqs. (11)–(15) are:

$$\text{On the inlet boundary : } u = (1, 0), \quad \theta = 0, \quad (16)$$

$$\text{On the outlet boundary : } P = 0, \quad (17)$$

$$\text{On the heated part of the bottom boundary : } \theta = 1, \quad (18)$$

$$\text{On the solid adiabatic (No slip condition) boundaries : } u = v = 0, \quad (19)$$

$$\text{On the solid flexible segment : } \left( \frac{\partial \theta}{\partial n} \right) = K_r \left( \frac{\partial \theta_s}{\partial n} \right), \quad (20)$$

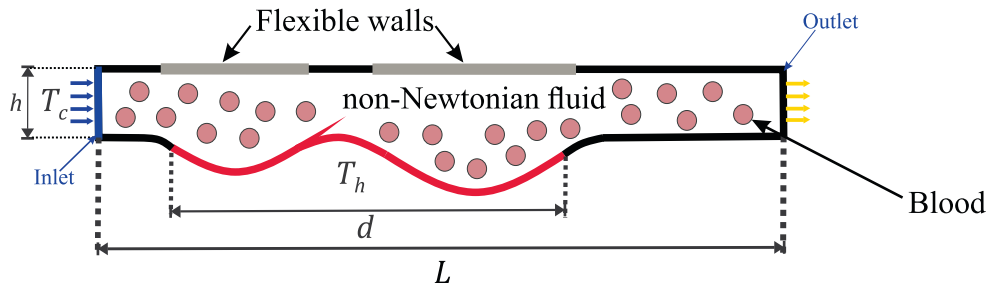


Fig. 1 2D schematic diagram of the physical model.

where  $K_r = \frac{k_s}{k_f}$ . Also, on the solid–fluid interface,

$$\frac{\partial d_s}{\partial t} = u \text{ and } \frac{E}{\rho_f \mu_{in}^2} \sigma \cdot \mathbf{n} = -P + \frac{D_{ij}}{Re} \nabla \mu_a. \quad (21)$$

The dimensionless initial temperature of the fluid and the fin is  $\theta = 0.5$ . The dimensionless initial velocity is  $u = 0$ . For the pressure point constraint, the following dimensionless pressure constraint is also considered:

$$P = 0 \quad (22)$$

In the present study, the parameter of interest is the Nusselt number, which shows the heat transfer from the wall. The local Nusselt number along at the hot wall is written as:

$$Nu = - \left( \frac{\partial \theta}{\partial \mathbf{n}} \right)_D, \quad (23)$$

here  $D$  is the total length of the heater where  $D = \frac{d}{L}$ .

The average Nusselt number at the basis of the abdominal segment can be introduced as:

$$\overline{Nu} = \frac{1}{D} \int_0^D Nu d\mathbf{n}. \quad (24)$$

The pressure drop across the channel ( $\Delta P$ ) can be obtained as:

$$\Delta P = P_{in} - P_{out}. \quad (25)$$

### 3. Numerical Method and Validation

The dimensionless governing equations subject to the selected boundary conditions are solved with the Galerkin weighted residual finite-element method. The computational domain is divided into sub-domains (finite elements) as shown in Fig. 2, and each of the velocity distribution, pressure and temperature are approximated by using basis set  $\{\Phi_j\}_{j=1}^M$  as,

$$\begin{aligned} \mathbf{V} &\approx \sum_{j=1}^M \mathbf{V}_j \Phi_j(X, Y), & P &\approx \sum_{j=1}^M P_j \Phi_j(X, Y), \\ \theta &\approx \sum_{j=1}^M \theta_j \Phi_j(X, Y). \end{aligned} \quad (26)$$

Fig. 3 shows the computational steps. The governing equations for the pressure, flow field, structure displacement, and the moving mesh are written in the weak form and integrated over the domain using the Gauss quadrature method to obtain the residual equations. Then, the residual equations are solved iteratively in a coupled scheme to obtain the field variables. A second-order backward differential formula (BDF) is employed to control the time step and relative computational error below  $10^{-4}$ . A view of the computational steps is depicted in Fig. 3. A non-uniform unstructured mesh was used in the domain of the solution. A fine mesh in the walls and next to the wall boundaries is applied to capture the field gradients better. The mesh study is performed to study the impact of mesh size on computational accuracy. For a coarse mesh, there are convergence issues. However, a fine mesh could stably capture the field gradients. A further reduction of the mesh size could not change the results but could increase the computational time. Thus, as depicted in Fig. 2, a fairly fine mesh is adopted for the computations.

The current research outcomes are validated against the report of Küttler and Wall [34]. They investigated the transient flow in an enclosure with an oscillating top lid while the bottom wall of the enclosure was flexible. The fluid’s kinematic viscosity and density were  $0.01 \text{ m}^2/\text{s}$  and  $1.0 \text{ kg}/\text{m}^3$ , respectively. The wall was 2 mm thick with a density and Young’s modulus of  $500 \text{ kg}/\text{m}^3$  and  $250 \text{ N}/\text{m}^2$ . Comparison with Küttler and Wall [34] for the case of the lid-driven domain, as shown in Fig. 4, shows the reliability of the present method. For a further validation, we pursued to conduct an experimental verification. Nevertheless, it was not possible to do this with a very close geometry. Thus, our attention is focused on a flow of water through a 3D microchannel incorporated with a flexible segment as a part of the upper wall of the microchannel. This geometry was studied numerically and experimentally by Chakraborty et al. [35]. The flexible segment was subjected to two influential parameters namely, the flow of water through the channel and a pressure (of air) applied externally on the flexible segment. The comparison was made with the amplitude of the deflected flexible segment as described in Fig. 5.

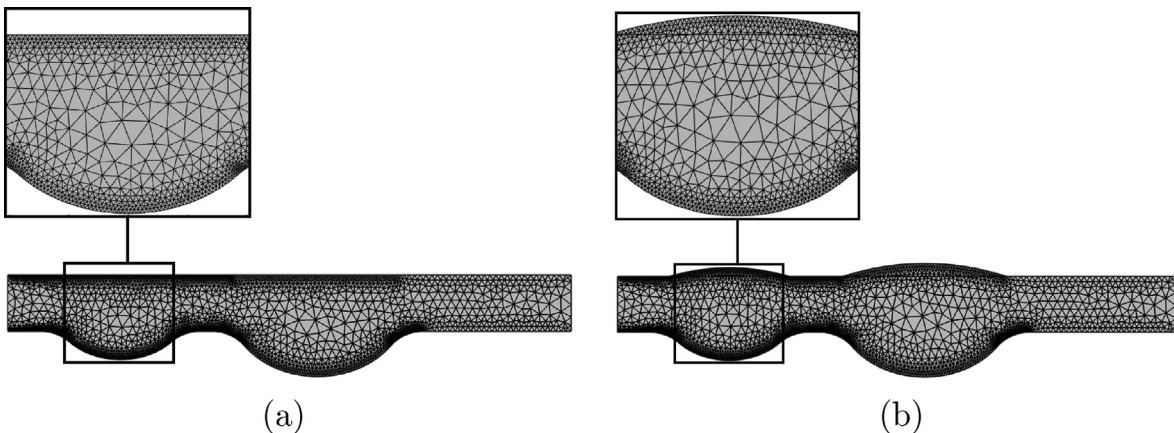


Fig. 2 (a) grid-points distribution at  $\tau = 0.001$  and (b) grid-points distribution at  $\tau = 10$ .

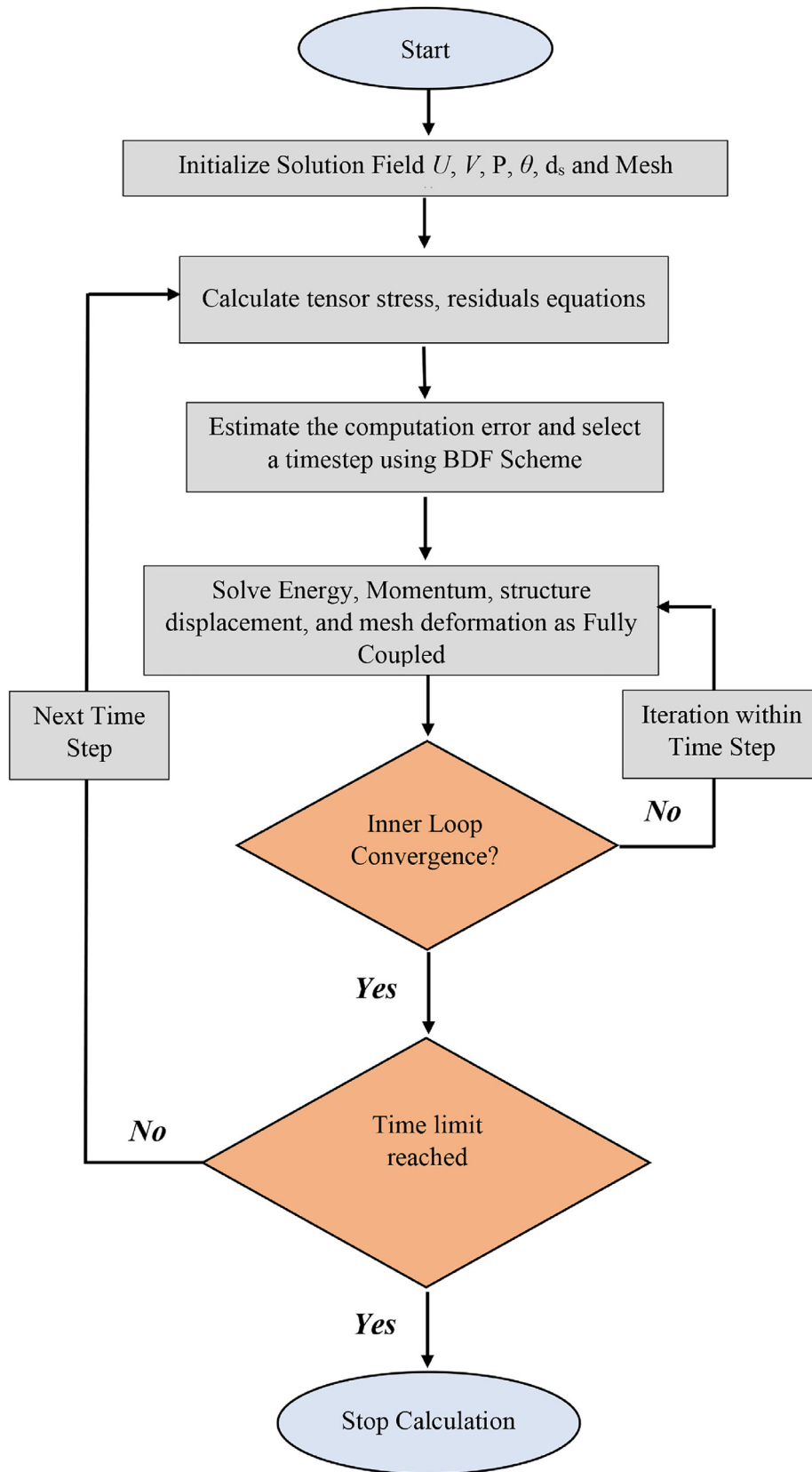
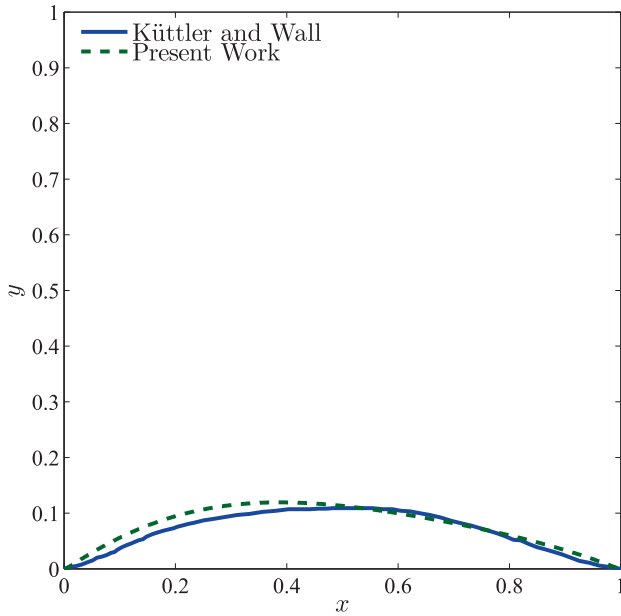
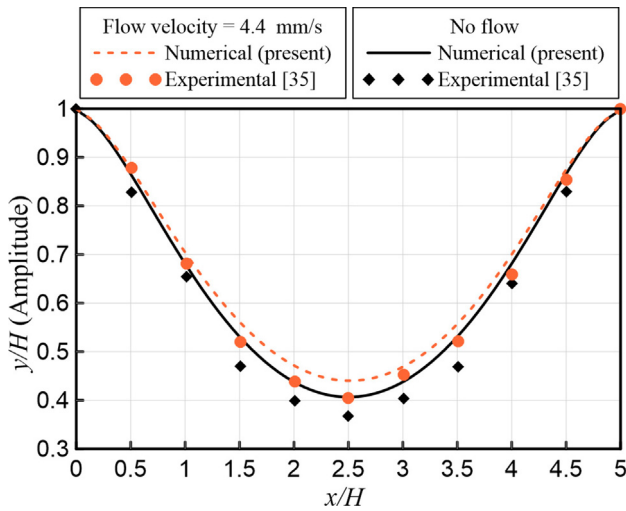


Fig. 3 A diagram of the computational steps.



**Fig. 4** The deformation curves of the deformable lower bound of the lid-driven enclosure examined by Küttler and Wall [34] and the present study. at  $t = 7.5s$ .



**Fig. 5** Comparison of the amplitude of the deflection of a flexible segment in a microchannel (Experimental study of Chakraborty et al. [35]).

#### 4. Results and Discussion

The considered geometry comprises double-aneurysms representing small and large lower bulges, and two flexible segments opposite to each aneurysm. To simulate the blood flow within this abdominal aortic aneurysm (AAA), the power-law index  $n$  is chosen within the shear thinning non-Newtonian fluid ( $0.2 \leq n \leq 0.8$ ) while the blood flow is considered constant and represented by the Reynolds number ( $50 \leq Re \leq 500$ ). The transient time of the numerical solution is inspected within ( $10^{-4} \leq \tau \leq 10^1$ ). The thermal conductivi-

ties of the blood and the walls are fixed at 0.52 and 1.45, respectively, while the elasticity of both flexible segments is set at  $10^{10}$ .

The progressions of the velocity and temperature are examined with time to inspect the transient period and the steady or time periodic state as depicted in Fig. 6 for  $Re = 100$  and  $n = 0.342$ . The velocity magnitude which is displayed using color scale is supported by streamlines also to visualize the generated recirculation. The figure tells that the streamlines stratify in streamwise pattern beyond the time 0.001, then ordered to fill most the passage, even inside the lower small and large bulges. Simultaneously, the first and the second flexible segments start to swell. The evolution of the streamlines and the swelling of the flexible segments reach the final shape at  $\tau = 10$ . At this state and owing to the diverging nature, the flow of the blood is weaker within the two bulges and close to the flexible segments. The development of the temperature contours also reaches its steady state at  $\tau = 10$  (Fig. 6(f)) which portrays hotter blood in the vicinity of the inner walls of the two aneurysms. This because the weak flow there is insufficient to convey the heat from the hot lower wall. Moreover, along the inner wall of both aneurysms, the thickness of thermal boundary layer adjacent to the descent part is higher than that of the ascent part. The direction of blood flow which opposes the ascent parts help in ejecting more thermal energy, i.e. the mixed convection is stronger, which is a good explanation for the variations of the thermal boundary thickness along the walls of the aneurysms. The evolutions of the average Nusselt number and the total distance of both swelling flexible segments for different Reynolds numbers (Fig. 7) and different power-law indices  $n$  (Fig. 8)) show that the transient variations exist up to  $\tau = 1$ , while at  $\tau = 10$  the steady state is completely attained. Hence, it is worth to assert that the steady state time is at  $\tau = 10$  and unless stated, the forthcoming results will be displayed at this time.

The impact of flow rate which is represented by the Reynolds number is depicted in Fig. 9 for  $n = 0.342$ . At a low  $Re$ , the streamlines look uniform and follow the entire geometry, leading to a uniform thermal boundary-layer thickness in both aneurysms with that of the large aneurysm which is thicker than the small aneurysm. This is because the inertial force at  $Re = 50$  is almost exhausted at the small bulge resulting in the existence of the temperature gradients even beyond the large aneurysm i.e. in the developing blood passage (Fig. 9(a)). Physically, the Reynolds number corresponds to a direct increase in the inertial forces capable to induce laminar flow for a fixed viscous fluid [36]. With this physical explanation, higher blood flow rates impose higher inertial forces and owing to the relatively low viscous forces, separation starts to form recirculated fluid zones when a sufficient space is available, namely in the large aneurysm as indicated in  $Re = 150$  (Fig. 9(b)). The recirculation expands evidently for higher  $Re$  numbers and occupies the entire space of the large lower bulge as can be seen in Fig. 9(d-e). In these situations, the streamlines are aligned in a uniform straight behavior in the regular horizontal vessel and on the other hand, a weak recirculation appears in the small bulge. The swelling of the two flexible segments is insensible with this figure. The temperature distributions for high  $Re$  values show the variations of the thermal boundary thickness in the descent and ascent walls of both lower bulges.

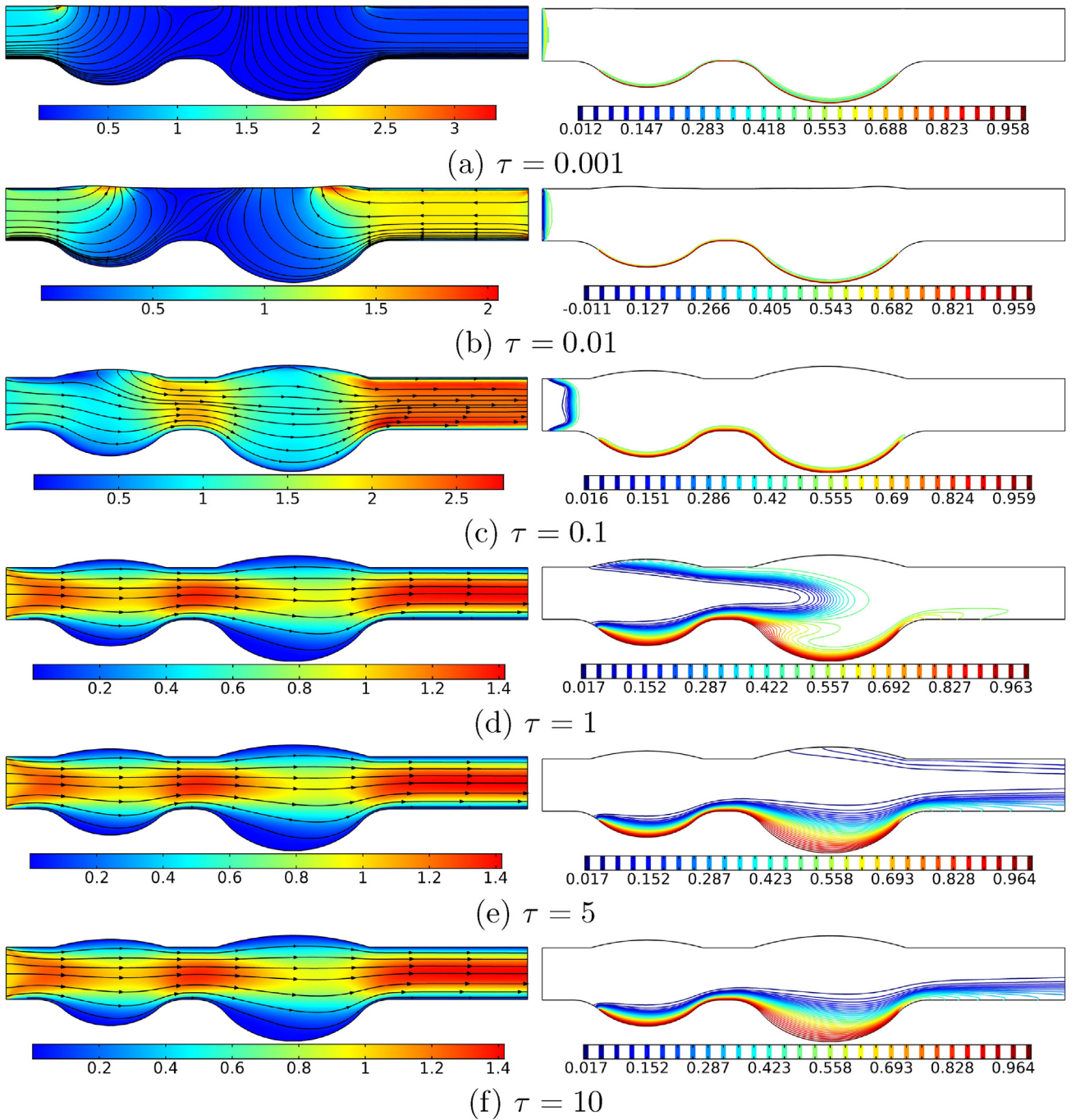


**Fig. 6** Variations of (left) velocity, (middle) streamlines, and (right) isotherms evolution by the dimensionless time ( $\tau$ ) for  $Re = 100$  and  $n = 0.342$ .

Although the heat is added across the lower wall of the aortic abdominal isothermally, the temperature gradient represented by the local Nusselt number varies sharply along the wall. This is mainly because of the wavy wall arising from the lower swells where the wake zones experience blood circulations. The blood circulation adds extra resistance to convective heat transfer; therefore the local Nusselt number drops along the descent and ascent segments as shown in Fig. 10(a) which depicts maximal values at the segment joining the two

aneurysms where the high blood velocity helps in ejecting more thermal energy. The figure portrays that the higher Reynolds number is the higher the peaks of the local Nusselt numbers, and at  $Re \geq 400$ , lower peaks exist within the small aneurysm due to the formation of the blood circulation at this range of  $Re$ . Without a close view of the local deflection of the first flexible segment, the impact of  $Re$  on its deformation may be omitted (Fig. 10(b)). However, the close view reveals a little wall shrinkage with  $Re$ . This can be referred to that the

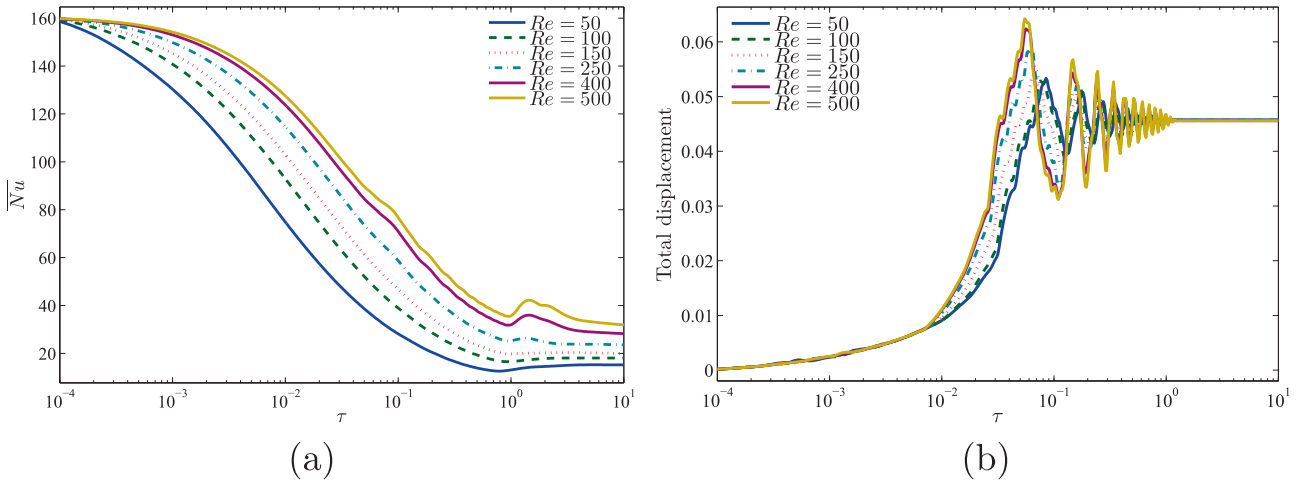


Fig. 7 Variations of (a) average Nusselt number and (b) total displacement with  $\tau$  for different  $Re$  at  $n = 0.342$ .

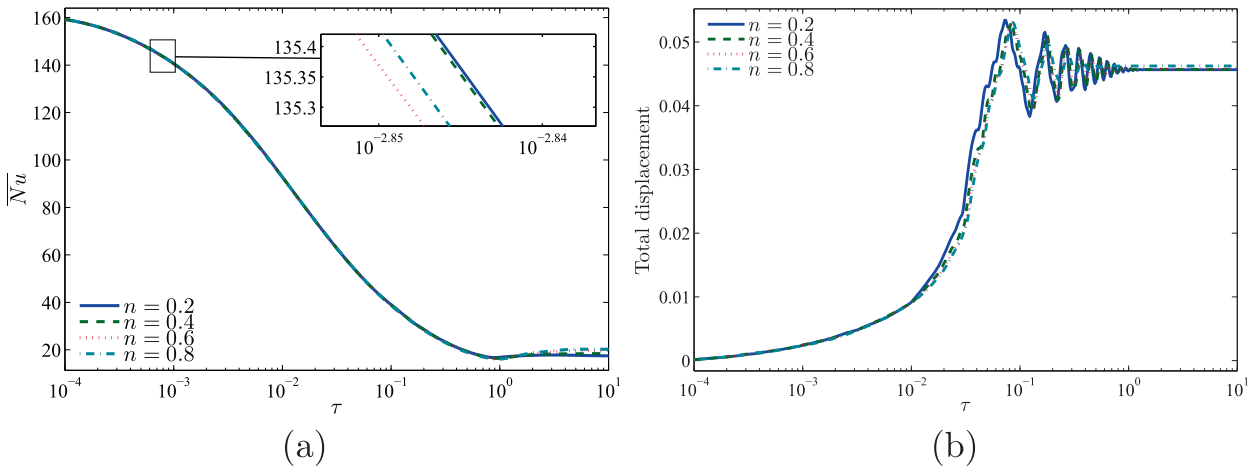


Fig. 8 Variations of (a) average Nusselt number and (b) total displacement with  $\tau$  for different  $n$  at  $Re = 100$ .

increase of the kinetic energy (dynamic pressure) is confronted by the decrease in potential energy (static pressure) exerted on the walls.

The oscillation of the velocity magnitude at  $Y = 0.2$  in Fig. 11(a) reflects the hydrodynamic effects of the bulges and the deflected flexible segments existing in the abdominal aortic. The lowest velocity magnitude is indicated at a situation opposite to the large aneurysm and for the lowest Reynolds number. Similarly, the local shear stress along the lower wall of the vessel oscillates in accordance with the undulations of the vessel walls (Fig. 11(b)), and showing inverse relation between the shear stress and the Reynolds number. The inverse relation refers to the shear thinning behavior of ( $n < 1$ ) and the reduction of the viscous force with increasing values of the Reynolds number.

The patterns of the streamlines and the temperature contours with the power-law index ( $n$ ) are presented in Fig. 12 for  $Re = 100$  and reveal the following. The circulation is seen with the lowest value of  $n$  namely at  $n = 0.2$  where the low apparent viscosity assists in blood flow separation. It can be deduced now that neither the Reynolds number nor the

power-law index have a noticeable influence on the deflection of the flexible walls, hence it is thought that the bulged nature of the abdominal aortic is behind the noted enlargement of the flexible segments. The temperature contours portray that the thermal boundary layer close to the hot wall becomes thinner with increasing values of  $n$  implying more heat transfer, and this is well known in the literature. Fig. 13(a) elucidates also a qualitative increase of the local Nusselt number with  $n$ . Fig. 13(b) reveals that with a larger value of  $n$ , there is a larger force acting on the flexible walls leading to swelling it out. The velocity magnitude at  $Y = 0.2$  is influenced by the value of  $n$  within the regions of a strong velocity namely, the regions of a regular vessel. That is, for a given Reynolds number, a fluid with a lower value of  $n$  exhibits a less apparent viscosity and therefore, a less viscous force. Conversely, the shear stress is much higher for a fluid with a higher value of  $n$  (Fig. 14(b)). Thus, it is strictly recommended to reduce the viscous nature of the blood in diseased vessels.

To get a qualitative and thorough look about the impacts of the power-law index and  $Re$ , the average Nusselt number and the total deflection of the two flexible segments are

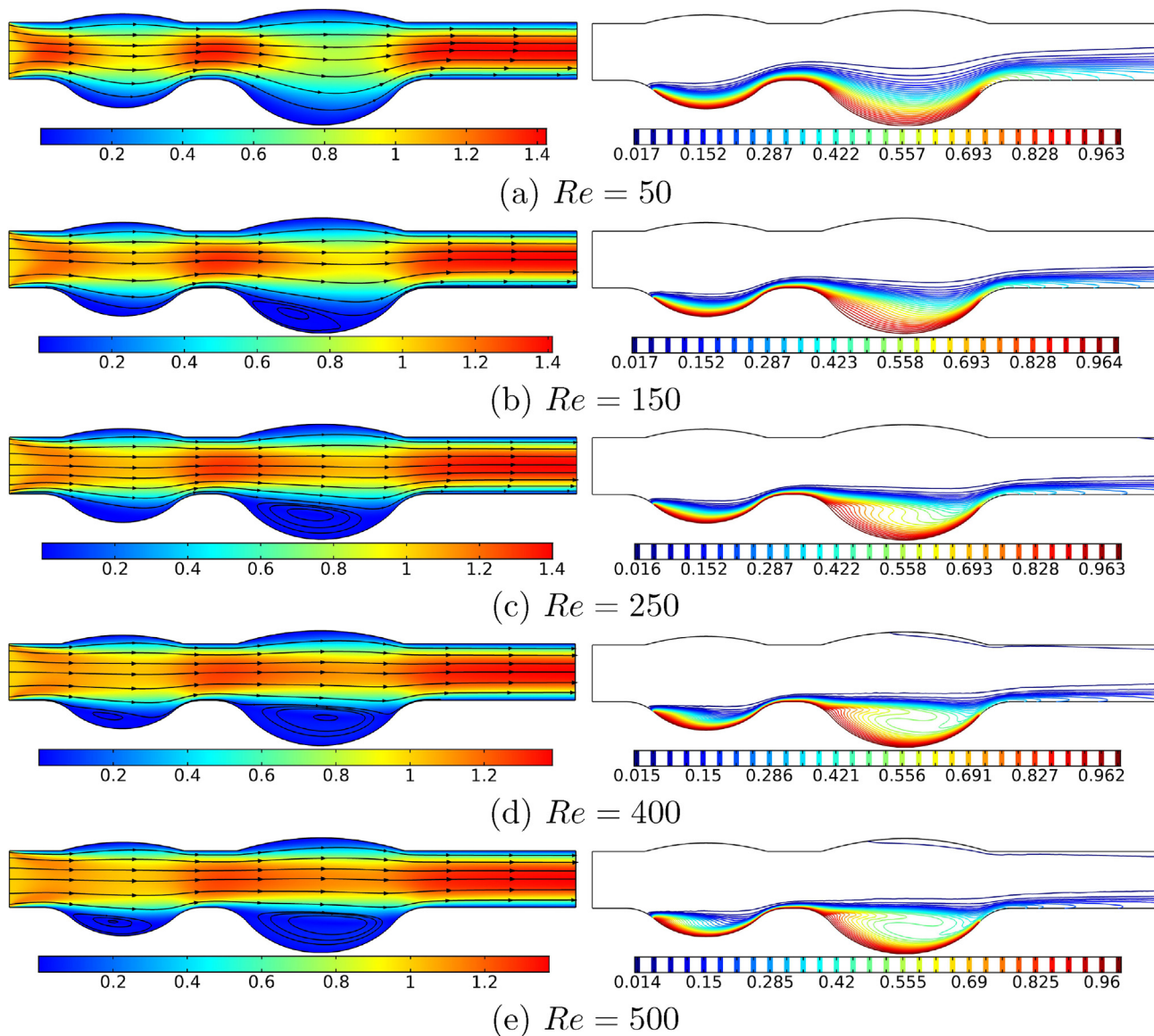


**Fig. 9** Variations of (left) velocity, (middle) streamlines, and (right) isotherms evolution by Reynolds number ( $Re$ ) for  $\tau = 10$  and  $n = 0.342$ .

inspected in Fig. 15. More heat energy can be transported to the blood at a higher Reynolds number (Fig. 15(a)). Conversely, the flexible wall segments shrink with  $Re$  and expand with  $n$  as shown in Fig. 15(b), however the impact of  $n$  dwindles at higher  $Re$  numbers. Keeping in mind that the impacts of  $n$  and  $Re$  on the deflection of the flexible walls are minor compared with the effect of geometry nature of the vessel. An extra explanation of the consequences of varying  $Re$  and  $n$  is shown graphically in Fig. 16 for the total pressure drop and the average temperature over the entire vessel. Because of the viscous force effect, the pressure drop dwindles with  $Re$  and rises with  $n$  as shown in Fig. 16(a). On the other hand,

the blood becomes hotter when both the Reynolds number and the power-law index are lowered as illustrated in Fig. 16(b).

## 5. Conclusions

Flow and heat transfer in a heated abdominal aortic aneurysm using an isothermal boundary condition has been investigated numerically using Arbitrary-Lagrangian-Eulerian (ALE) approach to simulate a thermal therapy. The Fluid-Structure Interaction (FSI) technique has been adopted and the blood is assumed a non-Newtonian fluid. Two unequal aneurysms forming lower two swells have been heated by a constant temperature

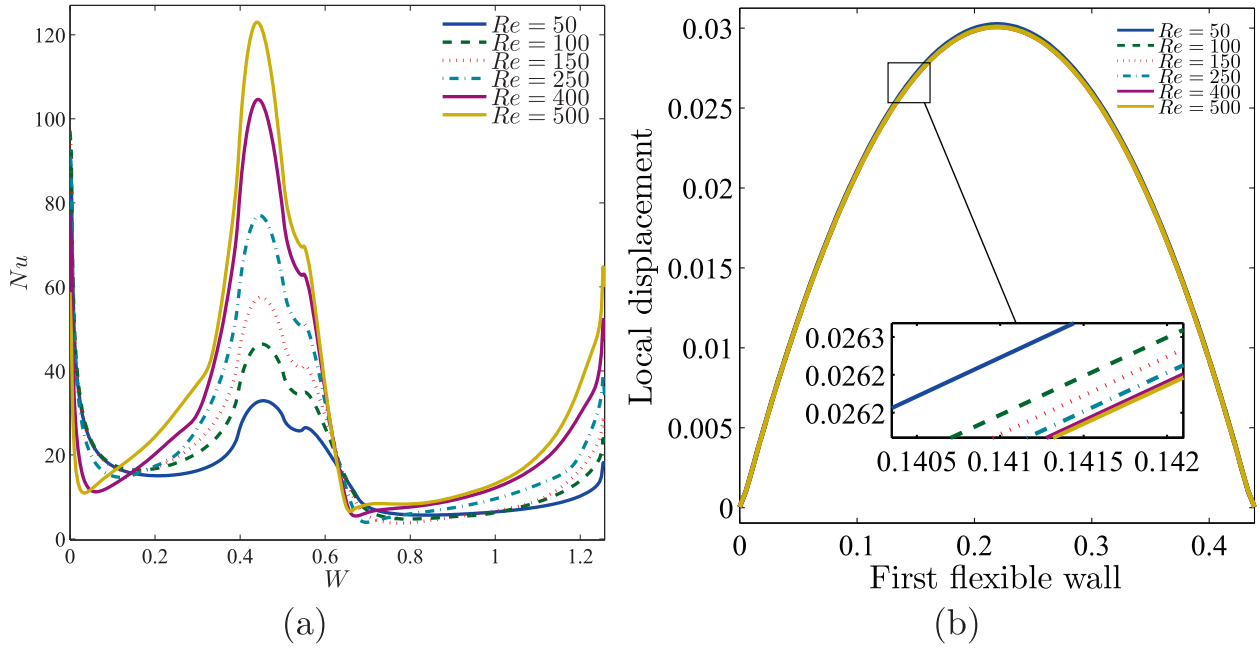


**Fig. 10** Variations of (a) local Nusselt number and the heated wall  $W$ , and (b) local displacement at the first flexible wall for different  $Re$  at  $\tau = 10$  and  $n = 0.342$ .

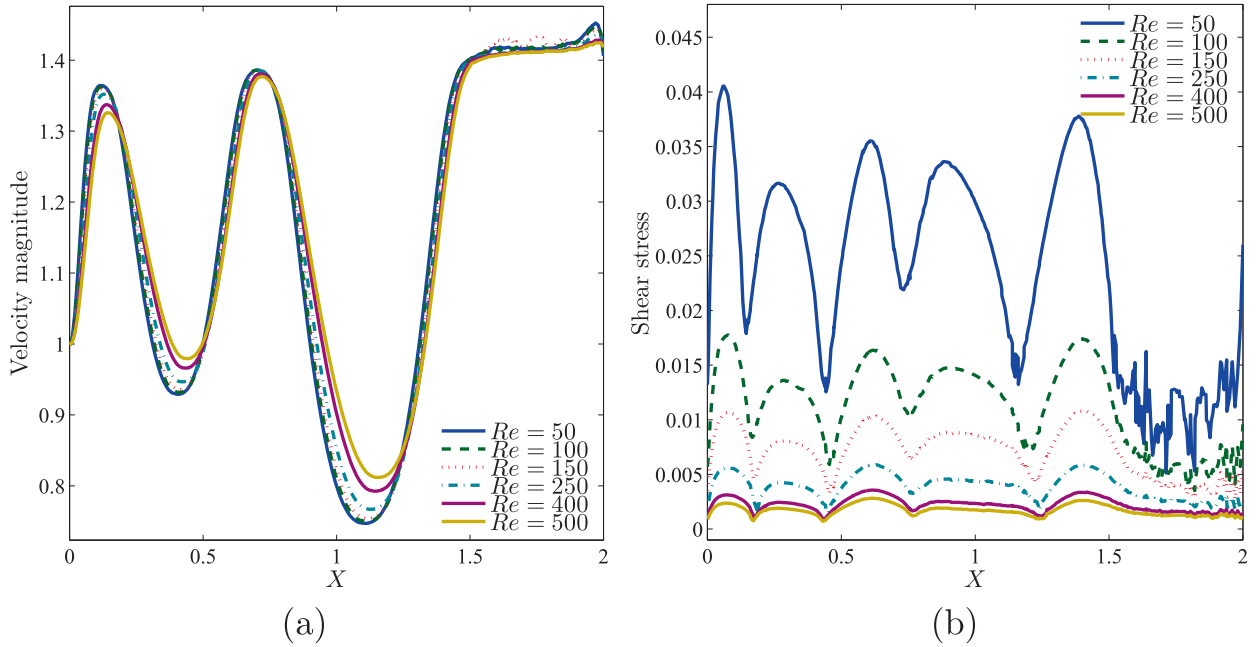


**Fig. 11** Variations of local (a) velocity and (b) shear stress with the horizontal axis  $X$  ( $Y = 0.2$ ) for different  $Re$  at  $\tau = 10$  and  $n = 0.342$ .

to simulate hyperthermia therapy. The upper wall segments opposing to each aneurysm has been taken flexible. This arrangement helps in understanding the integrity of the artery and how one can use heat as a thermic treatment. It is concluded that:

1. The shear stress is much higher for a higher index of the power-law fluid governing the blood viscosity and hence, it is strictly recommended to reduce the viscous nature of the blood in diseased vessels.

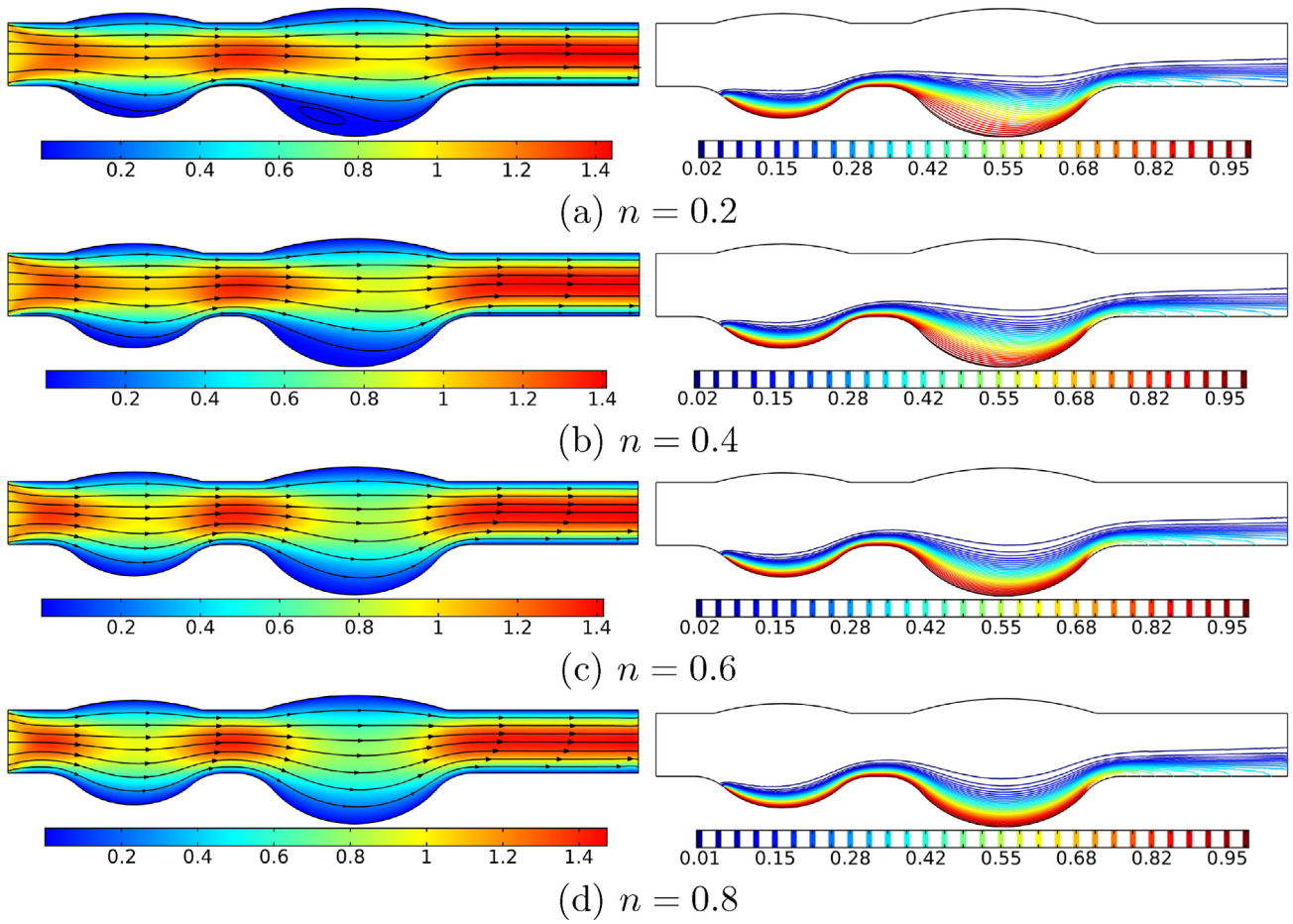


**Fig. 12** Variations of (left) velocity, (middle) streamlines, and (right) isotherms evolution by power-law index ( $n$ ) for  $\tau = 10$  and  $Re = 100$ .

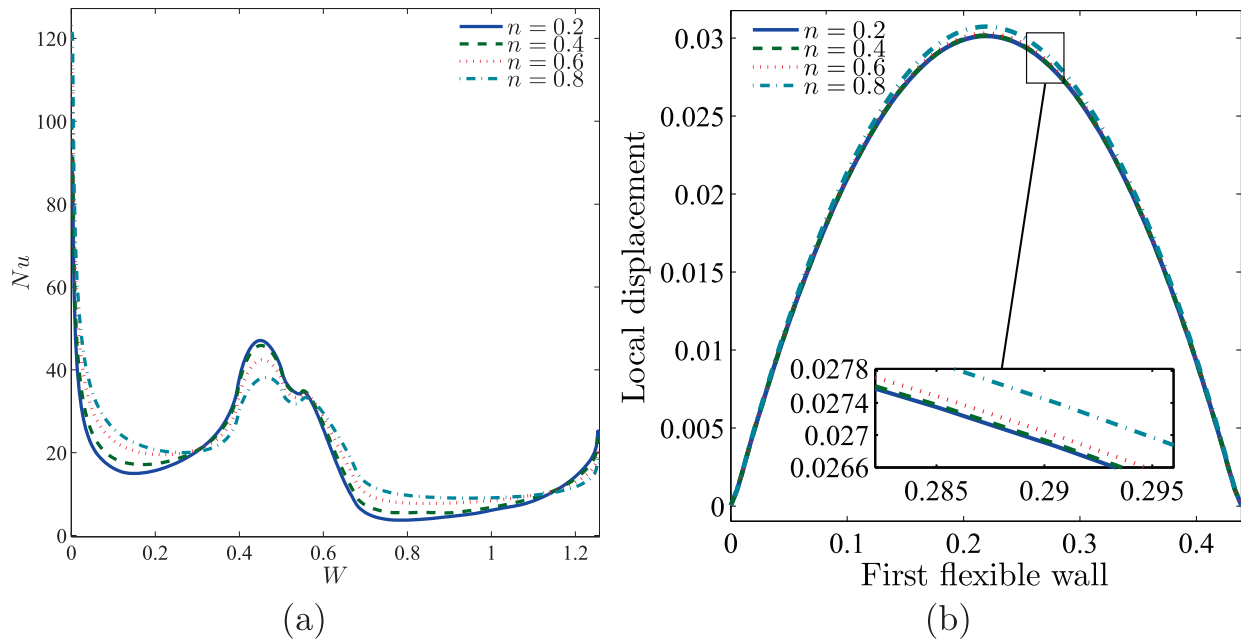


**Fig. 13** Variations of (a) local Nusselt number and the heated wall  $W$ , and (b) local displacement at the first flexible wall for different  $n$  at  $\tau = 10$  and  $Re = 100$ .

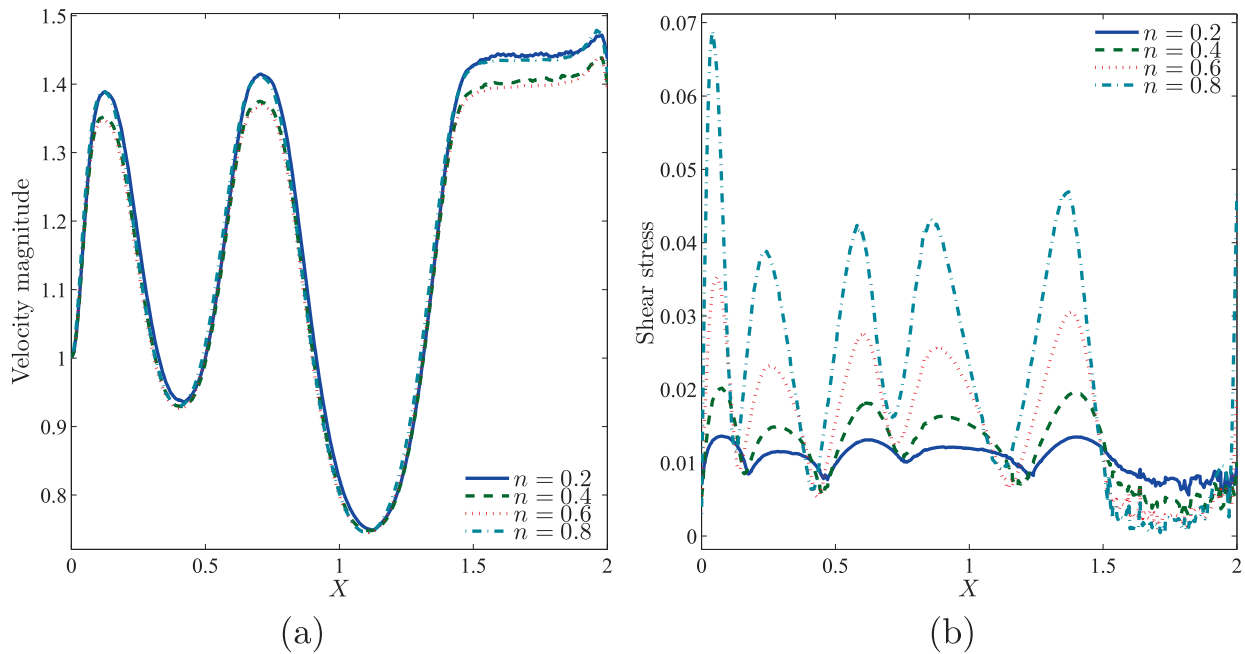


**Fig. 14** Variations of local (a) velocity and (b) shear stress with the horizontal axis  $X$  ( $Y = 0.2$ ) for different  $n$  at  $\tau = 10$  and  $Re = 100$ .

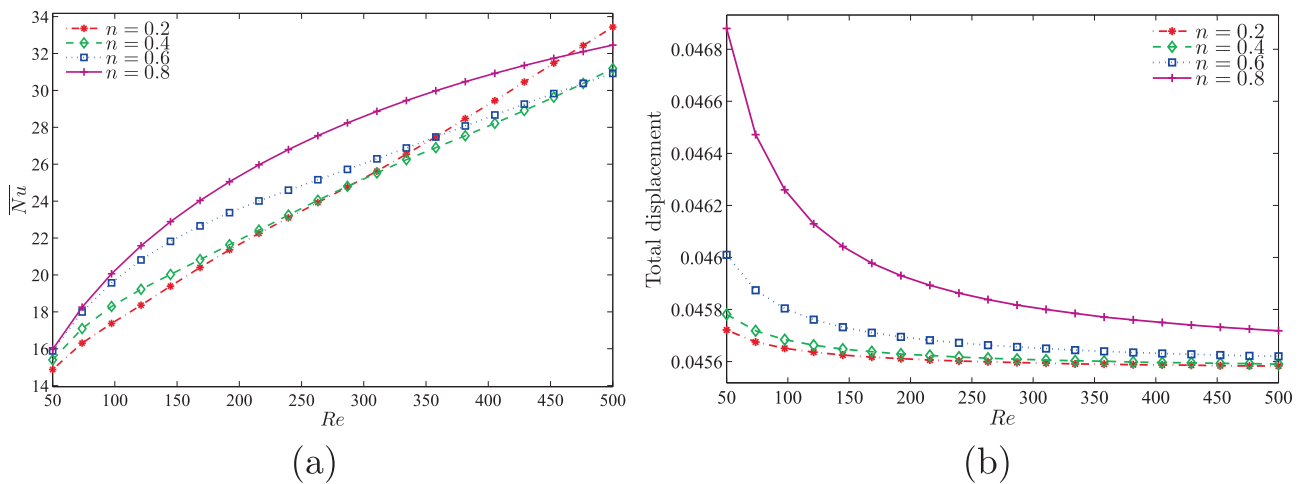


**Fig. 15** Variations of (a) average Nusselt number and (b) total displacement with  $Re$  for different  $n$  at  $\tau = 10$ .

2. The thermal energy can be transported across the blood significantly at a higher Reynolds number, this means that the hyperthermia therapy becomes effective when blood flows violently through the aortic.
3. The blood gets hotter at lower power-law index i.e. at low viscosity blood, the hyperthermia therapy becomes active.
4. Neither the Reynolds number nor the power-law fluid index have noticeable influence on the swelling of the flexible walls. However, it is asserted that the bulged nature of the abdominal aortic is behind the noted enlargement of the flexible segments.

5. The role of power-law fluid index dwindles at a higher Reynolds number. It is also concluded that the pressure drop across the entire studied vessel dwindles with the Reynolds number and rises with power-law fluid index, the reason behind heart harmful with high viscosity blood.

#### Declaration of Competing Interest

The authors declare that they have no known competing financial interests or personal relationships that could have appeared to influence the work reported in this paper.

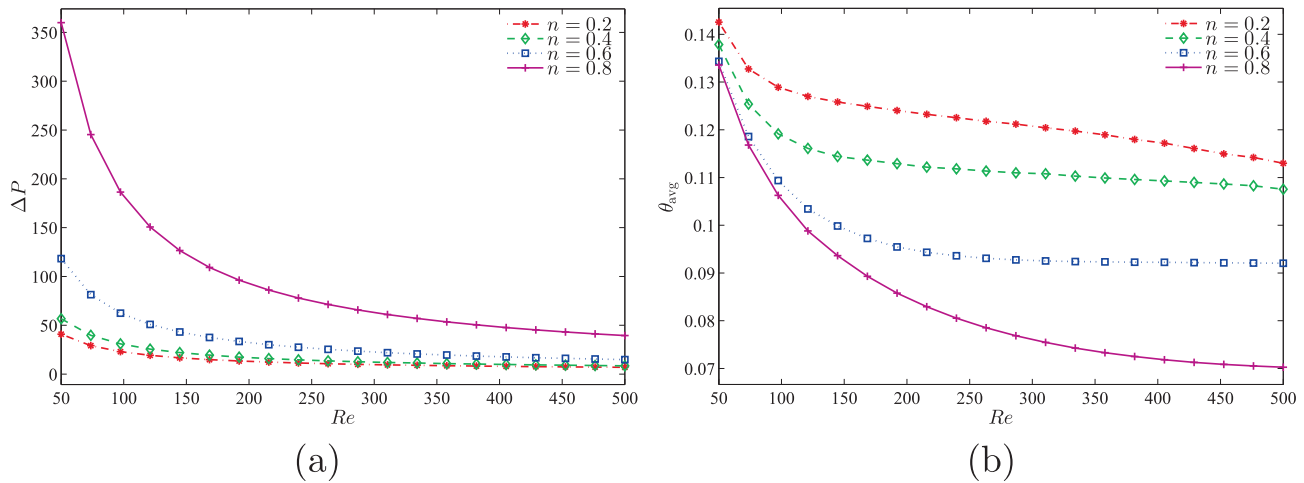


**Fig. 16** Variations of (a) pressure drop and (b) average temperature with  $Re$  for different  $n$  at  $\tau = 10$ .

### Acknowledgments

The work was supported by the Universiti Kebangsaan Malaysia (UKM) research grant GP-2021-K006388. We thank the respected reviewers for their constructive comments which clearly enhanced the quality of the manuscript. This research of Mohammad Ghalambaz was supported by the Tomsk State University Development Programme (Priority-2030).

### References

- [1] J.E. McCarroll, J.C. Denniston, D.R. Piere, L.J. Farese, Behavioral evaluation of a winter warfare training exercise. US Army Research Institute of Environmental Medicine, Report No 1977;1:78.
- [2] N. Asmuin, L.J. Xiong, M.S. Kamarudin, A. Mohammad, I. Taib, Heat distribution on abdominal aorta having aneurysm during hyperthermia therapeutic, *Res. Prog. Mech. Manuf. Eng.* 1 (1) (2020) 139–145.
- [3] K. Ouriel, R.M. Green, C. Donayre, C.K. Shortell, J. Elliott, J. A. DeWeese, An evaluation of new methods of expressing aortic aneurysm size: Relationship to rupture, *J. Vasc. Surg.* 15 (1) (1992) 12–20.
- [4] S.K. Al-Hadraawy, M.E. Al-ghurabi, M.M. Al-musawi, M. Alzeyadi, Ghrelin and melatonin as biomarkers in patients with giardiasis, *Biotechnol. Biotechnol. Equip.* 30 (3) (2016) 553–557.
- [5] Al-Hadraawy S.K., Alzeyadi M., Shakir A.A., noori Al-dujaili A. Detection of *Toxoplasma gondii* genotypes in abortion women by RFLP-PCR in Al-Najaf Al-Ashraf province. In: *Journal of Physics: Conference Series*; vol. 1234. IOP Publishing; 2019, p. 012084.
- [6] M. Saleem, Q.M. Al-Mdallal, Q.A. Chaudhry, S. Noreen, A. Haider, Partial slip effects on the peristaltic motion of an upper-convected Maxwell fluid through an irregular channel, *SN Appl. Sci.* 2 (5) (2020) 1–14.
- [7] R.E. Rosensweig, Heating magnetic fluid with alternating magnetic field, *J. Magn. Mater.* 252 (2002) 370–374.
- [8] A. Jordan, P. Wust, H. Fählín, W. John, A. Hinz, R. Felix, Inductive heating of ferrimagnetic particles and magnetic fluids: physical evaluation of their potential for hyperthermia, *Int. J. Hyperth.* 9 (1) (1993) 51–68.
- [9] A. Wakif, A novel numerical procedure for simulating steady MHD convective flows of radiative casson fluids over a horizontal stretching sheet with irregular geometry under the combined influence of temperature-dependent viscosity and thermal conductivity, *Mathematical Problems in Engineering* 2020 (2020).
- [10] M.U. Ashraf, M. Qasim, A. Wakif, M.I. Afridi, I.L. Animasaun, A generalized differential quadrature algorithm for simulating magnetohydrodynamic peristaltic flow of blood-based nanofluid containing magnetite nanoparticles: A physiological application, *Numerical Methods for Partial Differential Equations* 38 (3) (2022) 666–692.
- [11] A. Candeo, F. Dughiero, Numerical fem models for the planning of magnetic induction hyperthermia treatments with nanoparticles, *IEEE Trans. Magn.* 45 (3) (2009) 1658–1661.
- [12] H.G. Bagaria, D.T. Johnson, Transient solution to the bioheat equation and optimization for magnetic fluid hyperthermia treatment, *Int. J. Hyperth.* 21 (1) (2005) 57–75.
- [13] Y.G. Lv, Z.S. Deng, J. Liu, 3-D numerical study on the induced heating effects of embedded micro/nanoparticles on human body subject to external medical electromagnetic field, *IEEE Trans. Nanobiosci.* 4 (4) (2005) 284–294.
- [14] D. Su, R. Ma, M. Salloum, L. Zhu, Multi-scale study of nanoparticle transport and deposition in tissues during an injection process, *Medical & Biological Engineering & Computing* 48 (9) (2010) 853–863.
- [15] S. Saranya, Q.M. Al-Mdallal, Non-Newtonian ferrofluid flow over an unsteady contracting cylinder under the influence of aligned magnetic field, *Case Studies in Thermal Engineering* 21 (2020) 100679.
- [16] C. Midya, G.C. Layek, A.S. Gupta, T.R. Mahapatra, Magnetohydrodynamic viscous flow separation in a channel with constrictions, *J. Fluids Eng.* 125 (6) (2003) 952–962.
- [17] S. Majee, G.C. Shit, Numerical investigation of MHD flow of blood and heat transfer in a stenosed arterial segment, *J. Magn. Mater.* 424 (2017) 137–147.
- [18] U. HaKfeli, *Magnetism in medicine*, Wiley-VCH, New York, 1998.
- [19] T. Chinyoka, O.D. Makinde, Computational dynamics of arterial blood flow in the presence of magnetic field and thermal radiation therapy, *Advances in Mathematical Physics* 2014 (2014).
- [20] T.W. Taylor, T. Yamaguchi, Three-dimensional simulation of blood flow in an abdominal aortic aneurysm—steady and unsteady flow cases, *J. Biomech. Eng.* 116 (1) (1994) 89–97.
- [21] K.M. Khanafer, P. Gadhoke, R. Berguer, J.L. Bull, Modeling pulsatile flow in aortic aneurysms: Effect of non-Newtonian properties of blood, *Biorheology* 43 (5) (2006) 661–679.

- [22] E. Boutsianis, M. Guala, U. Olgac, S. Wildermuth, K. Hoyer, Y. Ventikos, et al. CFD and PTV steady flow investigation in an anatomically accurate abdominal aortic aneurysm, *J. Biomech. Eng.* 131 (1) (2009).
- [23] C. Kumawat, B.K. Sharma, Q.M. Al-Mdallal, M. Rahimi-Gorji, Entropy generation for MHD two phase blood flow through a curved permeable artery having variable viscosity with heat and mass transfer, *Int. Commun. Heat Mass Transfer* 133 (2022) 105954.
- [24] A. Wakif, M. Zaydan, A.S. Alshomrani, T. Muhammad, R. Sehaqui, New insights into the dynamics of alumina-(60% ethylene glycol+ 40% water) over an isothermal stretching sheet using a renovated Buongiorno's approach: A numerical GDQLM analysis, *Int. Commun. Heat Mass Transfer* 133 (2022) 105937.
- [25] P.A. Cosford, G.C. Leng, J. Thomas, Screening for abdominal aortic aneurysm, *Cochrane Database of Systematic Reviews* (2007) (2).
- [26] P.S. Basnyat, A.H.B. Biffin, L.G. Moseley, A.R. Hedges, M.H. Lewis, Mortality from ruptured abdominal aortic aneurysm in wales, *Br. J. Surg.* 86 (6) (1999) 765–770.
- [27] K.W. Johnston et al, Ruptured abdominal aortic aneurysm: Six-year follow-up results of a multicenter prospective study, *J. Vasc. Surg.* 19 (5) (1994) 888–900.
- [28] N. Sakalihasan, R. Limet, O.D. Defawe, Abdominal aortic aneurysm, *The Lancet* 365 (9470) (2005) 1577–1589.
- [29] Investigators U.K.E.T., Endovascular versus open repair of abdominal aortic aneurysm. *New England Journal of Medicine* 2010;362(20):1863–1871.
- [30] W.A. Sabbar, M.A. Ismael, M. Almudhaffar, Fluid-structure interaction of mixed convection in a cavity-channel assembly of flexible wall, *Int. J. Mech. Sci.* 149 (2018) 73–83.
- [31] M.A. Ismael, H.F. Jasim, Role of the fluid-structure interaction in mixed convection in a vented cavity, *Int. J. Mech. Sci.* 135 (2018) 190–202.
- [32] P.T. Griffiths, Flow of a generalised newtonian fluid due to a rotating disk, *J. Nonnewton. Fluid Mech.* 221 (2015) 9–17.
- [33] O.A. Abegunrin, I.L. Animasaun, N. Sandeep, Insight into the boundary layer flow of non-Newtonian Eyring-Powell fluid due to catalytic surface reaction on an upper horizontal surface of a paraboloid of revolution, *Alexandria Engineering Journal* 57 (3) (2018) 2051–2060.
- [34] U. Küttler, W.A. Wall, Fixed-point fluid–structure interaction solvers with dynamic relaxation, *Comput. Mech.* 43 (1) (2008) 61–72.
- [35] D. Chakraborty, J.R. Prakash, J. Friend, L. Yeo, Fluid-structure interaction in deformable microchannels, *Phys. Fluids* 24 (10) (2012) 102002.
- [36] I.L. Animasaun, N.A. Shah, A. Wakif, B. Mahanthesh, R. Sivaraj, O.K. Koriko, Ratio of momentum diffusivity to thermal diffusivity: Introduction, meta-analysis, and scrutinization, 2022.